Elsevier Editorial System(tm) for Earth and Planetary Science Letters
Manuscript Draft

Manuscript Number: EPSL-D-20-00417R2

Title: Carbon ordering in an aseismic shear zone: implications for Raman geothermometry and strain tracking

Article Type: Letters

Keywords: Raman spectroscopy; strain; carbon order; shear zone; geothermometry

Corresponding Author: Miss Lauren Kedar,

Corresponding Author's Institution: University of Aberdeen

First Author: Lauren Kedar

Order of Authors: Lauren Kedar; Clare Bond; David Muirhead

Abstract: Determining the burial and strain history of sedimentary rocks is important for understanding crustal behaviour. When rocks contain organic carbon, increased temperatures at depth can alter the molecular structure of the carbon. This change, known as carbon ordering, can be detected using Raman spectroscopy. As a result, Raman spectroscopy is increasingly used to estimate burial depths and associated maximum temperatures in carbon-bearing rocks. It is known from experiments and natural samples that other factors can affect Raman-derived maximum temperatures, including frictional heating on fault planes and interaction with hot fluids. For faulted samples, a question remains as to whether it is purely frictional heating that causes carbon ordering or strain, or a combination of the two. In this study, we use a mid-crustal shear zone to show that strain-related carbon ordering occurs in natural rock samples during aseismic shear strain. A traverse across the shear zone, whose relative strain we quantify with respect to the surrounding less deformed rock, shows a marked decrease in Raman D/G peak intensity ratios indicating greater carbon ordering within the shear zone. We interpret this as evidence for carbon ordering as a result of aseismic shear strain, rather than inflated temperatures, due to frictional heating commonly associated with seismic strain rates on faults. Our results have implications for the further development of Raman spectroscopy as a geothermometer (which may yield erroneous results in strained rock samples) and for understanding strain localisation processes in the Earth's crust, and its associated rheological implications.

Carbon ordering in an aseismic shear zone: implications for Raman geothermometry and strain tracking

Lauren Kedar[1]*, Clare E. Bond[1], David Muirhead[1]

[1]*School of Geosciences, University of Aberdeen, King's College, Aberdeen, AB24 3UE.*

*email: l.kedar@abdn.ac.uk

Keywords: Raman spectroscopy, geothermometry, strain, shear zone, organic carbon.

Abstract

Determining the burial and strain history of sedimentary rocks is important for understanding crustal behaviour. When rocks contain organic carbon, increased temperatures at depth can alter the molecular structure of the carbon. This change, known as carbon ordering, can be detected using Raman spectroscopy. As a result, Raman spectroscopy is increasingly used to estimate burial depths and associated maximum temperatures in carbon-bearing rocks. It is known from experiments and natural samples that other factors can affect Raman-derived maximum temperatures, including frictional heating on fault planes and interaction with hot fluids. For faulted samples, a question remains as to whether it is purely frictional heating that causes carbon ordering or strain, or a combination of the two. In this study, we use a mid-crustal shear zone to show that strain-related carbon ordering occurs in natural rock samples during aseismic shear strain. A traverse across the shear zone, whose relative strain we quantify with respect to the surrounding less deformed rock, shows a marked decrease in Raman D/G peak intensity ratios indicating greater carbon ordering within the shear zone. We interpret this as evidence for carbon ordering as a result of aseismic shear strain, rather than inflated temperatures, due to frictional heating commonly associated with seismic strain rates on faults. Our results have implications for the further development of Raman spectroscopy as a geothermometer (which may yield erroneous results in strained rock samples) and

for understanding strain localisation processes in the Earth's crust, and its associated rheological implications.

1. Introduction

Establishing the burial history of sedimentary sequences is important across a range of geological disciplines, including determining basin subsidence, rifting rates, and nappe stacking sequences in compressional regimes. One increasingly common method of estimating maximum burial is through Raman spectroscopy of carbon. As burial depth increases, fragments of organic carbon contained within the rock are altered on a molecular level, gradually progressing from an amorphous nanostructure (Thrower, 1989; Beyssac et al., 2002a; Rouzaud et al., 2015) to one with increased order, the end member of which is graphite (Wopenka and Pasteris, 1993; Beyssac et al., 2002b; Schito et al., 2017). This process is known as carbon ordering. Characteristics of Raman spectra depend on the extent of carbon ordering; this process is not reversed during exhumation, making Raman spectroscopy a key tool for establishing maximum burial depths and for deriving associated peak temperatures in organic carbon-bearing rocks (Tuinstra and Koenig, 1970; Landis, 1971; Nemanich and Solin, 1979; Knight and White, 1989; Ferrari and Robertson, 2001; Beyssac et al., 2002a; Muirhead et al., 2012, 2017b; Schito et al., 2017; Nibourel et al., 2018). Difficulties in deriving burial depths from Raman spectroscopy of organic carbon are compounded by potential influences from other crustal heat sources e.g. hydrothermal alteration (Large et al., 1994; Beyssac et al., 2002a), contact metamorphism (Muirhead et al., 2017a), as well as frictional heating due to seismic slip (Suchy et al., 1997; Oohashi et al., 2011; Yao et al., 2016; Kuo et al., 2017). For success, the user must distinguish burial temperature (associated with a regional geothermal gradient) from these other heat sources.

However, burial and crustal heat sources are not the only factors which influence carbon ordering. Recent experimental work has shown that strain has an effect (Kitamura et al., 2012; Kuo et al., 2014; Furuichi et al., 2015). The experimental work of those authors has primarily focused on the role of graphite on seismic fault slip surfaces, with less consideration of broader shear zones where strain may still be significant but distributed over a wider area, as in this study. Many studies only consider the effects of strain on graphite, and not on amorphous carbonaceous material: Raman spectroscopy of graphite on experimental slip surfaces (deforming at aseismic rates) show the graphite nanostructure to have been forcibly fragmented, inducing carbon disorder (e.g. Nakamura et al., 2015; Kirilova et al., 2018). In contrast, amorphous carbon (as addressed in this study) *orders* towards a graphitic nanostructure during seismic shear, due to high strain rates and frictional heating (Oohashi et al., 2011; Kitamura et al., 2012; Furuichi et al., 2015; Kuo et al., 2017). The presence of graphite on fault planes has therefore been purported as evidence of seismic slip (Oohashi et al., 2011; 2012; Rutter et al., 2013; Savage et al., 2014). But is the driver for carbon order elevated temperatures as a result of frictional heating, or a consequence of strain, or both?

In this study, we investigate a field example in which changes in Raman spectra spatially correlate with strain intensity across a distributed, aseismic shear zone. We chose an exhumed mid-crustal aseismic shear zone at the base of a 3100m thick stratigraphic section because it allows separation of burial effects from those associated with strain. An aseismic shear zone also ensures no influence on carbon order from the frictional heating associated with seismic faulting. Furthermore, our analysis focusses on amorphous carbon found in weakly metamorphosed (sub-greenschist facies) carbonates. Our work shows that carbon ordering occurs in an aseismic shear zone as a direct result of increased strain. We discuss the implications of this for the use of Raman spectroscopy to predict burial depths and peak temperatures in strained terranes. We also consider the potential effect of strain-induced carbon ordering in organic-rich layers on strain localisation in the mid-crust.

2. Geological Setting

The Haut Giffre, French Alps (Figure 1A), comprises a 3100m thick succession of thrust-stacked Tethyan shelf carbonates and shales, Middle Jurassic (Bajocian) to Late Cretaceous (Senonian) in age

(Figure 1B) (Collet, 1927; Dietrich and Durney, 1986; Butler, 2013). Compressional structures such as folds and large- and small-scale thrusts systems have a NNW vergence direction, compounded by foliation orientation. The complex thrusted/folded sequence is exposed in a series of cliff sections (Figure 1C). This paper focuses on a shear zone formed in the overturned limb of a recumbent fold structure within Bajocian marls, exposed in oblique cross-section around the Cirque du Fer à Cheval valley. The Bajocian is internally thickened by this NNW-verging, recumbent, isoclinal fold with a wavelength of 300m and amplitude of 1000m (Figure 1D, 2A). All strata in the fold dip SSE. The overturned limb is a shear zone characterized in the field by tight parasitic folds with wavelengths of 1-10m and interlimb angles <15°, and a strong, pervasive cleavage.

3. Methods

3.1. Strain Analysis

From a 400m transect through the fold, a total of 26 samples were collected across the upper, overturned (sheared), and lower limbs (Figure 2A). Of these, 19 thin sections were cut perpendicular to foliation, and the microstructure of the carbonate analyzed using optical microscopy and SEM (Figure 2B, 2C). The rock samples are predominantly calcite with minor clay and silicate content (Figure 2B, 2C). A strain ranking score system was developed based on three characteristics visible in a representative view under the optical microscope: (i) calcite elongation (Schmid et al., 1981; Kennedy and Logan, 1997), (ii) percentage grain alignment (Burkhard, 1990; Austin et al., 2008), and (iii) frequency of dissolution surfaces (Ferrill and Groshong, 1993; Ebert et al., 2007). Additionally, calcite twin type (I-IV) was used as a stress-strain indicator (Ferrill, 1991; Burkhard, 1993), to provide an independent test of the strain rank score. Strain data were collected from multiple 3 x 4 mm quadrangles on each thin section. The selected quadrangles were chosen for their representativeness of the entire section, after a visual inspection. The results of the strain data collected were then averaged. Calcite elongation measurements used the maximum aspect ratio of calcite grains in the field of view (Figure 3A); grain alignment was determined from the estimated percentage of grains or calcite twins occupying a dominant orientation (Figure 3B); dissolution surfaces were counted to give a number per mm (Figure 3C). To directly compare each factor, measurements were given a weighted score between 0 and 100, with 100 representing the most strained sample for that factor, and 0 representing no evidence of strain. The strain rank score was calculated for each thin section by summing the weighted values for each factor and normalizing (Equations 1 and 2) to give a relative score between 0 and 10, with 10 being the most deformed:

Equation 1: $$strain\ ranking\ score = \frac{\Sigma - \Sigma_{min}}{20.9} + 0.9091$$

In Equation 1, Σ is the sum of E+D+A (grain elongation (E), dissolution seam frequency (D), and grain alignment (A); see Table 1), and Σ_{min} is the lowest value of E+D+A in the complete dataset, which in this case is 75. As a result, inputting the Σ_{min} value applicable to the data, we can simplify the equation into Equation 2:

Equation 2: $$strain\ ranking\ score = 0.0478\,\Sigma - 2.677$$

Numerical constants in these equations are derived from values specific to the range of this dataset, in order to normalise the score into a scale of 0 to 10. As such, these constants would have to be adjusted for a dataset different maximum/minimum Σ values.

Additionally, calcite twin types were examined in each sample, providing an independent test of the strain rank score (Figure 3D).

3.2. Raman Spectroscopy

In addition to the 26 samples from the fold, a further 15 samples were taken through the 3100m thick stratigraphic succession from the top of the sequence (0m) to the sheared fold samples, which start at 2820m below the top of the sequence. Sampling through the succession was carefully managed to avoid strained material (e.g. faults or shear zones) when outside of the sheared fold.

All samples were subsequently prepared for Raman spectroscopy. Owing to their relatively low total organic carbon (TOC) content (0.04-0.50%), the samples were prepared by crushing and treating with HCl to remove excess calcite, leaving the organic material behind. The crushing process lasted around 10 seconds and was consistent for all samples. The interested reader is referred to Henry et al. (2019) for a thorough review of preparation methods for Raman spectroscopy and their respective limitations.

Raman spectroscopy was performed using a Renishaw InVia Raman Spectrometer at the University of Aberdeen. A 514nm laser was targeted at individual grains in the residual powders, where the laser power was <3mW at the sample, and spot size was 1-2μm. Each run comprised three lots of 5-second acquisitions; this was carried out on 10 individual grains from each sample. Analysis of the spectra (Figure 4A) uses two spectral peaks at ~1350 cm^{-1} and ~1585 cm^{-1}. The former (1350cm^{-1}) is commonly known as D1, but for simplicity is referred to in this study as the D-peak. The intensity of the D-peak increases as the amorphous carbon structure breaks down into smaller molecular fragments at the early stages of the carbon-ordering process. The latter (1585cm^{-1}) is referred to in this study as the G-peak, but is in reality a combination of two first order Raman bands known as G and D2, the difference between which is negligible at low maturity (Beyssac et al., 2002b). The intensity of the G-peak increases in the later stages of carbon ordering, as the carbon nanostructure becomes more sheet-like.

The relative intensities of the D- and G-peaks (peak intensity ratio, I[d]/I[g]) is used to ascertain the extent to which carbon ordering has progressed. In the early stages of carbon ordering, usually due to burial, the molecular breakdown of kerogen produces an increase in I[d]/I[g] as the D-peak intensity increases but the G-peak intensity remains constant. As carbon ordering progresses further, the fragmented organic carbon orders into a more sheet-like structure and hence the G-peak intensifies, causing I[d]/I[g] to decrease again (Muirhead et al., 2012, 2017b; Buseck and Beyssac, 2014). This is usually caused by high temperature metamorphism (>600°C; e.g. Bustin et al., 1995; Furuichi et al., 2015). In this study, the samples have not undergone high-temperature metamorphism, since they are sub-greenschist facies, and hence have only progressed as far as the breakdown of kerogen due to burial (Figure 4B). For each sample, 10 spectra were acquired, and each of these spectra underwent smoothing, baseline removal, and curve fitting three times (Figure 2A). As a result, 30 I[d]/I[g] ratios were attributed to each sample (full dataset given in Supplementary Information).

4. Results

Scores and ranks for each of the 19 thin sections are given in Table 1. Figure 2 shows characteristic microstructures from the upper and overturned limbs of the sheared fold. Figure 2B, sample 17046 from the fold's upper limb, has the lowest strain rank score (0.91), a grain aspect ratio of 1:1.2, ~40% grain alignment, and 4.5 dissolution surfaces per mm. Figure 2C, sample 17011 from the overturned limb, has the highest strain rank score (10.0), a high grain aspect ratio (1:3), 90% alignment, and 15 dissolution surfaces per mm. Calcite twin type I-IV (Ferrill, 1991; Burkhard, 1993) provided a test of the strain rank score (Table 1, columns 5 and 14). Calcite grains in all thin sections exhibited Type II or III twins (Figure 3D). Samples from the overturned sheared limb exhibited Type III twinning (with one grain in one thin section showing Type IV), with no incidences of Type II. All samples in the upper and lower limbs show Type II twinning (except two samples which each had one grain showing Type III).

The Raman spectra results across the sheared fold are placed into the context of the change in Raman spectra with depth (burial) in the stratigraphic succession. Figure 5 shows Raman spectra I[d]/I[g] plotted against depth through the stratigraphy. Data from the sample sites was projected along strike onto the cross-section line (Figure 1C), with care taken to maintain the relative depth position of individual samples within the stratigraphy, before plotting as depth. From the top of the exposed stratigraphic pile (0m) to a depth of 2450m, I[d]/I[g] ratios range from 0.35 to 0.45 (Figure 5). At greater depths the I[d]/I[g] ratio increases from 0.39 to 0.69. Where the transect crosses the fold at a depth of 2820m, I[d]/I[g] ratios in the upper and lower limbs fit this burial trend, increasing to 0.89 at a depth of 3100m. However, in the sheared overturned limb, a sharp decrease in I[d]/I[g] ratios to 0.35-0.72 is recorded, diverging from this burial trend.

In Figure 6A we compare the change in Raman spectra I[d]/I[g] ratios across the sheared fold to the strain rank score devised for the carbonate samples. The strain rank score is divided into three subsets in the figure that define, relative to each other, low (0-3.99, green), medium (4.00-5.99, amber) and high (6.00-10.00, red) strain samples, and the sample locations on a schematic projection of the fold. Strain in the upper and lower limbs is relatively low with an average score of 2.08, and a range of 0.91 to 4.14. Figure 6C shows the median I[d]/I[g] values of the upper, overturned, and lower limbs to be 0.73, 0.65, and 0.83 respectively. The overturned sheared fold limb has medium to high relative strains with an average of 6.10, and ranging from 4.26 to 10.0. In Figure 6B the strain data and the Raman spectra I[d]/I[g] ratios are co-plotted, the upper and lower limbs have higher average Raman spectra I[d]/I[g] ratios (0.843 and 0.821 respectively) with a wider range (standard deviation = 0.178) than the sheared overturned limb (I[d]/I[g] = 0.649, standard deviation = 0.048); a difference of 23% (Figure 6B). The decreased I[d]/I[g] ratios in the sheared overturned limb correlate with higher strain rank scores and evidence of greater strain on calcite crystal axes in the form of Type III twins (Figure 6B).

5. Discussion

5.1. Deviation from burial trend

Figure 5 shows the overall change in I[d]/I[g] with depth through the thrust-stacked stratigraphic sequence; despite some localised variation, there is a clear trend towards increasing values at greater burial depths. At low metamorphic grades, such as the sub-greenschist facies that exists here, gradual increases in temperature (e.g. due to deeper burial) result in breakdown of kerogen. This raises the relative intensity of the D-peak, thus also raising the I[d]/I[g] ratio with increased depth (Sawatzki, 1974; Dietrich and Casey, 1989; Sauerer et al., 2017; Schito et al., 2017; Muirhead et al., 2017b). By placing the shear zone data in the context of the burial trend, it is clear that the

I[d]/I[g] values from the upper and lower limbs of the fold lie on this trend, whilst those in the sheared fold limb deviate significantly. Here we discuss three possible mechanisms for the deviation towards lower I[d]/I[g] values in the overturned limb: lower peak temperature, higher peak temperature, and increased strain.

5.2. Anomalously low peak temperature

In general terms, there are several reasons as to why I[d]/I[g] ratios may be lower than expected in a rock of low metamorphic grade. The simplest explanation is that the rock may have experienced a peak temperature which was lower than that of the surrounding rock (e.g. Beyssac et al, 2002; Muirhead et al., 2012). This can be achieved by faulting and/or folding. In the case of the fold here, the upper and lower limbs show higher I[d]/I[g] than the sheared overturned limb which lies in between them. Folded isotherms (e.g. Girault et al., 2019) do not explain the I[d]/I[g] pattern; the fold is too tight and the amplitude too low for a such a significant I[d]/I[g] decrease in the overturned limb to be accounted for by this mechanism. Further, the pattern of likely higher temperatures through lower temperatures (in the overturned limb), back to higher temperatures in the lower limb do not make sense in terms of folding deeper (presumably hotter) temperature material into the fold. As a result, it is unlikely that the I[d]/I[g] decrease in the overturned limb can be explained by lower peak temperatures in that limb.

5.3. Locally high peak temperature

We can also discount the role of high temperatures in reducing I[d]/I[g] in the overturned limb. At very high temperatures (600-900°C), carbon molecules begin to order into sheets without the addition of strain (e.g. Bustin et al., 1995; Furuichi et al., 2015; Kaneki et al., 2016). As a result, these studies correctly cite a temperature increase as a means of decreasing the I[d]/I[g] value. However, such temperatures are not applicable to our study, as the rocks remain within the sub-greenschist facies. Additionally, by choosing a shear zone that has deformed aseismically, we remove the possibility that the observed carbon ordering is the result of frictional heating, since an instantaneous slip of >2m would be required to generate such a large increase in temperature (Savage et al., 2014; Kaneki et al., 2016). Therefore, the observed I[d]/I[g] decrease in the overturned limb cannot be explained by increased temperatures in that limb.

5.4. Localised strain-related ordering

Experimental data of Kwiecinska et al. (2010), Kitamura et al. (2012) and Furuichi et al. (2015) suggest that shear strain can result in a decreased I[d]/I[g] ratio due to strain-related carbon ordering. Specifically, these experiments deal with seismic slip rates, but there is no reason that this mechanism cannot also apply to aseismic shear. With increasing strain, molecules of disordered organic carbon (high I[d]/I[g]) are mechanically aligned into sheets, increasing the G-peak and hence decreasing the I[d]/I[g] value. In our study, we quantify the relative intensity of carbonate strain fabrics across a sheared fold, allowing direct comparison between these strain indicators and I[d]/I[g] values. On average, our strain rank score (in which higher values indicate greater strain) yielded average values of 2.08 in the upper/lower limbs, and 6.10 in the overturned limb. These values correspond to average I[d]/I[g] ratios of 0.83 for the upper/lower limbs, and 0.65 for the overturned limb. There is minor overlap between I[d]/I[g] values in the upper limb and the overturned limb, but the median values shift significantly between limbs (Figure 6c). Further, those samples within the upper limb with lower I[d]/I[g] values show evidence of localised increased strain e.g. Type III calcite twins (Figure 3). The correlation between lower I[d]/I[g] values and consistent evidence of increased strain, combined with the experimental evidence of previous studies mentioned above, suggests that organic carbon in the shear zone (the overturned limb) may have undergone strain-related ordering.

5.5. Further considerations

Throughout the fold and the complete stratigraphic sequence, there is a spread of I[d]/I[g] values which typically span +/- 0.1 for any given stratigraphic level, including within the fold. As a result, it is important to consider overall trends rather than any one given value, and to focus on the shift in the range of values between the differing fold limbs. Localised variation can be a result of minor changes in one or all of the above factors. Despite efforts to minimise the effects of these factors at the chosen sample sites rocks are inherently heterogeneous, and this emphasises the need for multiple samples at each locality in future studies using Raman spectroscopy, as well as the need for careful sampling and associated strain analysis.

Our results have important implications for the development of Raman geothermometry. Most Raman-based temperature calculations involve I[d]/I[g] or peak area ratios (closely related to I[d]/I[g]) as a significant term in the equation (Lahfid, 2010; Schito and Corrado, 2018; Muirhead et al., 2019). Therefore, if such equations are utilised in deformed terranes, erroneous results are likely; in this case temperatures in the overturned limb would have been underestimated. This conclusion supports the work of Kirilova et al. (2018), who suggest that peak temperatures on faults may be underestimated by up to 300°C, citing field examples from New Zealand, Japan and the Carpathians (Nakamura et al., 2015; Barzoi, 2015; Kirilova et al., 2018).

Additionally, using the correlation between strain and I[d]/I[g], we can infer that zones of high strain contain a higher proportion of 'ordered' carbon, i.e. organic carbon that has been mechanically aligned into a sheet-like arrangement. Based on findings from previous studies (e.g. Krabbendam et al., 2003; Vauchez and Tommasi, 2003; Herwegh and Pfiffner, 2005; Upton and Craw, 2008), we infer that this may have rheological implications. Specifically, strain-related ordering could further localise deformation, in turn causing strain-related carbon ordering to progress further, and so on. Additionally, Nakamura et al. (2015) report accumulations of graphite (of sedimentary origin) within shear bands, through chemical enhancement. Further research is required to establish the precise impact of strain localisation processes driven by mechanical ordering, and at what carbon content such mechanical ordering may begin to have an effect. In experiments on seismically sheared synthetic fault gouges containing graphite, Rutter et al. (2013) highlight the importance of small volumes of graphite in maintaining weakness on the fault. This suggests that sheet-like, ordered carbon may play a role in the localisation of strain due to its mechanical anisotropy (Vauchez et al., 1997; Vauchez and Tommasi, 2003; Upton and Craw, 2008).

6. Conclusions

We have shown that a decrease in Raman spectra I[d]/I[g] ratios correlate with increased strain within a sheared overturned limb of a carbonate fold. The decrease corresponds to increases in calcite grain elongation, grain alignment, and frequency of solution seams, as well as a change from Type II to Type III calcite twinning. We use these factors as proxies for strain intensity, and conclude that the sheared, overturned fold limb experienced higher strain than the upper/lower fold limbs. This zone of increased strain correlates exactly with a distinct decrease in I[d]/I[g] across the overturned fold limb, suggesting that Raman intensity ratios and strain are linked.

Our study shows that I[d]/I[g] values in the sheared, overturned limb of the fold deviate significantly from the burial trend. Through this, we have separated and quantified the effects of strain-related carbon ordering from burial in an aseismic shear zone. Our data confirms the existence of strain-related carbon ordering in nature. This is consistent with the experimental data of Kwiecinska et al. (2010), Kitamura et al. (2012), Furuichi et al. (2015) and Kuo et al. (2017). Targeting a mid-crustal aseismic shear zone allows us to not only separate the burial signature from the influence of strain, but also from frictional heating. This distinction has not been elucidated in seismic shear experiments.

7. Implications

Raman geothermobarometric techniques are actively being developed (Ruiz Cruz, 2016; Kirilova et al., 2018b; Nibourel et al., 2018; Muirhead et al., 2019). Understanding the impact on Raman spectra of strain-related carbon ordering is critical to the development of these techniques and accurate determination of pressures and temperatures at a range of conditions. Our results suggest that the use of Raman spectroscopy as a geothermometer may not be appropriate in samples which have undergone differential strain, or in those where the strain history is not known. In this case, temperatures in the overturned limb would be underestimated using established Raman geothermometric calculations (e.g. Lahfid et al., 2010; Schito and Corrado, 2018). Additionally, our observations open up the possibility of using carbon order as a means of tracking strain, provided the effects of strain can be reliably isolated from temperature.

The relative anisotropy of a sheet-like carbon nanostructure has been noted as having a weakening effect on the host rock (Rutter et al., 2013). From our observations we suggest that total organic carbon and its distribution in a layered sedimentary sequence could influence deformation localization as strain accumulates and carbon ordering progresses.

8. Summary

We have shown that carbon ordering can occur naturally within aseismic shear zones, highlighting the need for dense and contextual sampling strategies when Raman spectroscopy is used to determine peak temperatures in deformed terranes. Our work emphasizes the need for further research into the role of strain-related ordering in a range of carbon-bearing materials for geothermometry, and on the controls on carbon ordering resulting from strain in aseismic shear zones.

Acknowledgements

This study was carried out as part of a University of Aberdeen PhD, supported by the NERC (Natural Environment Research Council) Centre for Doctoral Training in Oil & Gas [grant number NE/R01051X/1].

References

Austin, N., Evans, B., Herwegh, M., and Ebert, A., 2008, Strain localization in the Morcles nappe (Helvetic Alps, Switzerland): Swiss Journal of Geosciences, v. 101, p. 341–360, doi:10.1007/s00015-008-1264-2.

Beyssac, O., Goffé, B., Chopin, C., and Rouzaud, J.N., 2002a, Raman spectra of carbonaceous material in metasediments: a new geothermometer: Journal of Metamorphic Geology, v. 20, p. 859–871, doi:10.1046/j.1525-1314.2002.00408.x.

Beyssac, O., Rouzaud, J.-N., Goffé, B., Brunet, F., and Chopin, C., 2002b, Graphitization in a high-pressure, low-temperature metamorphic gradient: a Raman microspectroscopy and HRTEM study: Contributions to Mineralogy and Petrology, v. 143, p. 19–31, doi:10.1007/s00410-001-0324-7.

Burkhard, M., 1993, Calcite twins, their geometry, appearance and significance as stress-strain markers and indicators of tectonic regime: a review: Journal of Structural Geology, v. 15, p. 351–368, doi:10.1016/0191-8141(93)90132-T.

Burkhard, M., 1990, Ductile deformation mechanisms in micritic limestones naturally deformed at low temperatures (150–350°C): Geological Society, London, Special Publications, v. 54, p. 241–257, doi:10.1144/GSL.SP.1990.054.01.23.

Buseck, P.R., and Beyssac, O., 2014, From Organic Matter to Graphite: Graphitization: Elements, v. 10, p. 421–426, doi:10.2113/gselements.10.6.421.

Bustin, R.M., Ross, J.V., and Rouzaud, J.-N., 1995, Mechanisms of graphite formation from kerogen: experimental evidence: International Journal of Coal Geology, v. 28, p. 1–36, doi:10.1016/0166-5162(95)00002-U.

Butler, R.W.H., 2013, Area balancing as a test of models for the deep structure of mountain belts, with specific reference to the Alps: Journal of Structural Geology, v. 52, p. 2–16, doi:10.1016/J.JSG.2013.03.009.

Collet, L.W., 1927, The Structure of the Alps: London, Edward Arnold & Co.

Dietrich, D., and Casey, M., 1989, A new tectonic model for the Helvetic nappes: Geological Society, London, Special Publications, v. 45, p. 47–63, doi:10.1144/GSL.SP.1989.045.01.03.

Dietrich, D., and Durney, D.W., 1986, Change of direction of overthrust shear in the Helvetic nappes of western Switzerland: Journal of Structural Geology, v. 8, p. 389–398, doi:10.1016/0191-8141(86)90057-X.

Ebert, A., Herwegh, M., and Pfiffner, A., 2007, Cooling induced strain localization in carbonate mylonites within a large-scale shear zone (Glarus thrust, Switzerland): Journal of Structural Geology, v. 29, p. 1164–1184, doi:10.1016/j.jsg.2007.03.007.

Ferrari, A.C., and Robertson, J., 2001, Resonant Raman spectroscopy of disordered, amorphous, and diamondlike carbon: Physical Review B, v. 64, p. 075414, doi:10.1103/PhysRevB.64.075414.

Ferrill, D.A., 1991, Calcite twin widths and intensities as metamorphic indicators in natural low-temperature deformation of limestone: Journal of Structural Geology, v. 13, p. 667–675, doi:10.1016/0191-8141(91)90029-I.

Ferrill, D.A., and Groshong, R.H., 1993, Deformation conditions in the northern Subalpine Chain, France, estimated from deformation modes in coarse-grained limestone: Journal of Structural Geology, v. 15, p. 995–1006, doi:10.1016/0191-8141(93)90172-7.

Furuichi, H., Ujiie, K., Kouketsu, Y., Saito, T., Tsutsumi, A., and Wallis, S., 2015, Vitrinite reflectance and Raman spectra of carbonaceous material as indicators of frictional heating on faults: Constraints from friction experiments: Earth and Planetary Science Letters, v. 424, p. 191–200, doi:10.1016/J.EPSL.2015.05.037.

Girault, J.B., Bellahsen, N., Boutoux, A., Rosenberg, C.L., Nanni, U., Verlaguet, A., and Beyssac, O., 2020, The 3-D Thermal Structure of the Helvetic Nappes of the European Alps: Implications for Collisional Processes: Tectonics, v. 39, doi:10.1029/2018TC005334.

Henry, D. G., Jarvis, I., Gillmore, G. and Stephenson, M., 2019, Raman spectroscopy as a tool to determine the thermal maturity of organic matter: Application to sedimentary, metamorphic and structural geology: Earth Science Reviews, v. 198, p. 102936, doi:10.1016/j.earscirev.2019.102936.

Herwegh, M., and Pfiffner, O.A., 2005, Tectono-metamorphic evolution of a nappe stack: A case study of the Swiss Alps: Tectonophysics, v. 404, p. 55–76, doi:10.1016/j.tecto.2005.05.002.

Kaneki, S., Hirono, T., Mukoyoshi, H., Sampei, Y., and Ikehara, M., 2016, Organochemical characteristics of carbonaceous materials as indicators of heat recorded on an ancient plate-subduction fault: Geochemistry, Geophysics, Geosystems, v. 17, p. 2855–2868, doi:10.1002/2016GC006368.

Kennedy, L.A., and Logan, J.M., 1997, The role of veining and dissolution in the evolution of fine-grained mylonites: the McConnell thrust, Alberta: Journal of Structural Geology, v. 19, p. 785–797, doi:10.1016/S0191-8141(97)00005-9.

Kirilova, M. et al., 2018a, Textural changes of graphitic carbon by tectonic and hydrothermal processes in an active plate boundary fault zone, Alpine Fault, New Zealand: Geological Society, London, Special Publications, v. 453, p. 205–223, doi:10.1144/SP453.13.

Kirilova, M., Toy, V., Rooney, J.S., Giorgetti, C., Gordon, K., and Colletini, C., 2018b, Structural disorder of graphite and implications for graphite thermometry.: Solid Earth, v. 9, p. 223–231.

Kitamura, M., Mukoyoshi, H., Fulton, P.M., and Hirose, T., 2012, Coal maturation by frictional heat during rapid fault slip: Geophysical Research Letters, v. 39, p. n/a-n/a, doi:10.1029/2012GL052316.

Knight, D.S., and White, W.B., 1989, Characterization of diamond films by Raman spectroscopy: Journal of Materials Research, v. 4, p. 385–393, doi:10.1557/JMR.1989.0385.

Krabbendam, M., Urai, J.L., and van Vliet, L.J., 2003, Grain size stabilisation by dispersed graphite in a high-grade quartz mylonite: An example from Naxos (Greece): Journal of Structural Geology, v. 25, p. 855–866, doi:10.1016/S0191-8141(02)00086-X.

Kuo, L.-W., Di Felice, F., Spagnuolo, E., Di Toro, G., Song, S.-R., Aretusini, S., Li, H., Suppe, J., Si, J., and Wen, C.-Y., 2017, Fault gouge graphitization as evidence of past seismic slip: Geology, v. 45, p. 979–982, doi:10.1130/G39295.1.

Kuo, L.-W., Li, H., Smith, S.A.F., Di Toro, G., Suppe, J., Song, S.-R., Nielsen, S., Sheu, H.-S., and Si, J., 2014, Gouge graphitization and dynamic fault weakening during the 2008 Mw 7.9 Wenchuan earthquake: Geology, v. 42, p. 47–50, doi:10.1130/G34862.1.

Kwiecinska, B., Suárez-Ruiz, I., Paluszkiewicz, C., and Rodriques, S., 2010, Raman spectroscopy of selected carbonaceous samples: International Journal of Coal Geology, v. 84, p. 206–212, doi:10.1016/J.COAL.2010.08.010.

Lahfid, A., Beyssac, O., Deville, E., Negro, F., Chopin, C., and Goffé, B., 2010, Evolution of the Raman spectrum of carbonaceous material in low-grade metasediments of the Glarus Alps (Switzerland): Terra Nova, v. 22, p. 354–360, doi:10.1111/j.1365-3121.2010.00956.x.

Landis, C.A., 1971, Graphitization of dispersed carbonaceous material in metamorphic rocks: Contributions to Mineralogy and Petrology, v. 30, p. 34–45, doi:10.1007/BF00373366.

Large, D.J., Christy, A.G., and Fallick, A.E., 1994, Poorly crystalline carbonaceous matter in high grade metasediments: implications for graphitisation and metamorphic fluid compositions: Contributions to Mineralogy and Petrology, v. 116, p. 108–116, doi:10.1007/BF00310693.

Mostefaoui, S., Perron, C., Zinner, E., and Sagon, G., 2000, Metal-associated carbon in primitive chondrites: Structure, isotopic composition, and origin: Geochimica et Cosmochimica Acta, v. 64, p. 1945–1964, doi:10.1016/S0016-7037(99)00409-3.

Muirhead, D.K., Bond, C.E., Watkins, H., Butler, R.W.H., Schito, A., Crawford, Z., and Marpino, A., 2019, Raman Spectroscopy: an effective thermal marker in low temperature carbonaceous fold-thrust belts: Geological Society, London, Special Publications, p. SP490-2019–27, doi:10.1144/sp490-2019-27.

Muirhead, D.K., Bowden, S.A., Parnell, J., and Schofield, N., 2017a, Source rock maturation owing to igneous intrusion in rifted margin petroleum systems: Journal of the Geological Society, v. 174, p. 979–987, doi:10.1144/jgs2017-011.

Muirhead, D.K., Parnell, J., Spinks, S., and Bowden, S.A., 2017b, Characterization of organic matter in the Torridonian using Raman spectroscopy: Geological Society, London, Special Publications, v. 448, p. 71–80, doi:10.1144/SP448.2.

Muirhead, D.K., Parnell, J., Taylor, C., and Bowden, S.A., 2012, A kinetic model for the thermal evolution of sedimentary and meteoritic organic carbon using Raman spectroscopy: Journal of Analytical and Applied Pyrolysis, v. 96, p. 153–161, doi:10.1016/J.JAAP.2012.03.017.

Nakamura, Y., Oohashi, K., Toyoshima, T., Satish-Kumar, M., and Akai, J., 2015, Strain-induced amorphization of graphite in fault zones of the Hidaka metamorphic belt, Hokkaido, Japan: Journal of Structural Geology, v. 72, p. 142–161, doi:10.1016/J.JSG.2014.10.012.

Nemanich, R.J., and Solin, S.A., 1979, First- and second-order Raman scattering from finite-size crystals of graphite: Physical Review B, v. 20, p. 392–401, doi:10.1103/PhysRevB.20.392.

Nibourel, L., Berger, A., Egli, D., Luensdorf, N.K., and Herwegh, M., 2018, Large vertical displacements of a crystalline massif recorded by Raman thermometry: Geology, v. 46, p. 879–882, doi:10.1130/G45121.1.

Oohashi, K., Hirose, T., Kobayashi, K., and Shimamoto, T., 2012, The occurrence of graphite-bearing fault rocks in the Atotsugawa fault system, Japan: Origins and implications for fault creep: Journal of Structural Geology, v. 38, p. 39–50, doi:10.1016/J.JSG.2011.10.011.

Oohashi, K., Hirose, T., and Shimamoto, T., 2011, Shear-induced graphitization of carbonaceous materials during seismic fault motion: Experiments and possible implications for fault mechanics: Journal of Structural Geology, v. 33, p. 1122–1134, doi:10.1016/J.JSG.2011.01.007.

Pasteris, J.D., 1989, In Situ Analysis in Geological Thin-Sections by Laser Raman Microprobe Spectroscopy: A Cautionary Note: Applied Spectroscopy, v. 43, p. 567–570, doi:10.1366/0003702894202878.

Rouzaud, J.-N., Deldicque, D., Charon, É., and Pageot, J., 2015, Carbons at the heart of questions on energy and environment: A nanostructural approach: Comptes Rendus Geoscience, v. 347, p. 124–133, doi:10.1016/J.CRTE.2015.04.004.

Ruiz Cruz, M.D., 2016, Characterization of natural carbon particles formed at low temperature UHP conditions: Diamond and Related Materials, v. 61, p. 76–90, doi:10.1016/J.DIAMOND.2015.11.013.

Rutter, E.H., Hackston, A.J., Yeatman, E., Brodie, K.H., Mecklenburgh, J., and May, S.E., 2013, Reduction of friction on geological faults by weak-phase smearing: Journal of Structural Geology, v. 51, p. 52–60, doi:10.1016/J.JSG.2013.03.008.

Salver-Disma, F., Tarascon, J.M., Clinard, C., and Rouzaud, J.N., 1999, Transmission electron microscopy studies on carbon materials prepared by mechanical milling: Carbon, v. 37, p. 1941–1959, doi:10.1016/S0008-6223(99)00059-7.

Sauerer, B., Craddock, P.R., AlJohani, M.D., Alsamadony, K.L., and Abdallah, W., 2017, Fast and accurate shale maturity determination by Raman spectroscopy measurement with minimal sample preparation: International Journal of Coal Geology, v. 173, p. 150–157, doi:10.1016/J.COAL.2017.02.008.

Savage, H.M., Polissar, P.J., Sheppard, R., Rowe, C.D., and Brodsky, E.E., 2014, Biomarkers heat up during earthquakes: New evidence of seismic slip in the rock record: Geology, v. 42, p. 99–102, doi:10.1130/G34901.1.

Sawatzki, G., 1974, Etude géologique et minéralogique des flyschs à grauwackes volcaniques du synclinal de Thônes (Haute-Savoie, France) : grès de Taveyanne et grès du val d’Illiez:, https://tel.archives-ouvertes.fr/tel-00819767/ (accessed April 2019).

Schito, A., and Corrado, S., 2018, An automatic approach for characterization of the thermal maturity of dispersed organic matter Raman spectra at low diagenetic stages: Geological Society, London, Special Publications, v. 484, p. SP484.5, doi:10.1144/sp484.5.

Schito, A., Romano, C., Corrado, S., Grigo, D., and Poe, B., 2017, Diagenetic thermal evolution of organic matter by Raman spectroscopy: Organic Geochemistry, v. 106, doi:10.1016/j.orggeochem.2016.12.006.

Schmid, S.M., Casey, M., and Starkey, J., 1981, The microfabric of calcite tectonites from the Helvetic Nappes (Swiss Alps): Geological Society Special Publication, v. 9, p. 151–158, doi:10.1144/GSL.SP.1981.009.01.13.

Suchy, V., Frey, M., and Wolf, M., 1997, Vitrinite reflectance and shear-induced graphitization in orogenic belts: A case study from the Kandersteg area, Helvetic Alps, Switzerland: International Journal of Coal Geology, v. 34, p. 1–20, doi:10.1016/S0166-5162(97)00018-9.

Thrower, P., 1989, Chemistry and physics of carbon : a series of advances. . V. 22, in Marcel Dekkker, p. 247, https://books.google.co.uk/books?hl=en&lr=&id=LxRO3C-1uXYC&oi=fnd&pg=PA1&dq=high+resolution+tem+studies+carbonization+graphitization&ots=hh-K2zLv2l&sig=efQ16QIp_AKPs9g1kM3MDIr1Mqk#v=onepage&q=high resolution tem studies carbonization graphitization&f=fals (accessed February 2019).

Tuinstra, F., and Koenig, J.L., 1970, Raman Spectrum of Graphite: The Journal of Chemical Physics, v. 53, p. 1126–1130, doi:10.1063/1.1674108.

Upton, P., and Craw, D., 2008, Modelling the role of graphite in development of a mineralised mid-crustal shear zone, Macraes mine, New Zealand: Earth and Planetary Science Letters, v. 266, p. 245–255, doi:10.1016/j.epsl.2007.10.048.

Vauchez, A., Barruol, G., and Tommasi, A., 1997, Why do continents break-up parallel to ancient orogenic belts? Terra Nova, v. 9, p. 62–66, doi:10.1111/j.1365-3121.1997.tb00003.x.

Vauchez, A., and Tommasi, A., 2003, Wrench faults down to the asthenosphere: Geological and geophysical evidence and thermomechanical effects: Geological Society Special Publication, v. 210, p. 15–34, doi:10.1144/GSL.SP.2003.210.01.02.

Wopenka, B., and Pasteris, J.D., 1993, Structural characterization of kerogens to granulite-facies graphite: Applicability of Raman microprobe spectroscopy: American Mineralogist, v. 78, p. 533–557.

Yao, L., Ma, S., Platt, J.D., Niemeijer, A.R., and Shimamoto, T., 2016, The crucial role of temperature in high-velocity weakening of faults: Experiments on gouge using host blocks with different thermal conductivities: Geology, v. 44, p. 63–66, doi:10.1130/G37310.1.

Figure Captions

Figure 1: An overview of the geology of the Haut Giffre field area. (A) Regional setting of the Haut Giffre within the Alpine Chain. (B) Regional stratigraphy (Jurassic-Cretaceous) (C) Geological map of the Haut Giffre and surrounding peaks (major ridgelines marked in dark grey). Sample locations are marked by open circles. Orientation data represent local averages of 2-15 nearby strike/dip measurements. Location of cross-section X-Y is marked by a black line. (D) SE-NW cross-section X-Y. The fold structure considered in this study is indicated by the box.

Figure 2: Photographs of outcrop exposure and thin sections. (A) Stitched photograph montage of the fold structure in the Cirque du Fer a Cheval valley. The cliff section is oriented approximately SW-NE. Red lines indicate bedding traces. The fold hinge, between the upper and overturned limb, is marked in yellow. Note that the fold is verging approximately NNW and is cut obliquely by the cliff face, resulting in the apparent change in bed thickness across the hinge. The lower limb cannot be seen in this image. Parasitic folds in the overturned limb are visible on the right-hand side of the image. (B(i)) Photomicrograph of sample 17046, taken from the upper limb, showing sinuous dissolution seams (4.5 surfaces per mm) and remnant depositional texture, with 40% calcite twin

alignment. (B(ii)) SEM image of sample 17046, showing rounded grains of calcite, quartz, and a small amount of organic carbon. (C(i)) Photomicrograph of sample 17011, taken from the overturned limb, showing strong mineral alignment and 15 dissolution seams per mm. Calcite twins cannot be clearly seen in these images. (C(ii)) SEM image of 17011, showing strong grain alignment.

Figure 3: Schematic representation of strain indicators and typical thin section photomicrographs. (A(i)) poorly-aligned, low aspect ratio grains; (B(i)) elongate, well-aligned grains; (C(i)) clearly visible dissolution seams. In parts (A), (B) and (C), (ii) shows photomicrographs of samples exhibiting the characteristics represented in part (i). (D) Photomicrographs of samples exhibiting (i) Type II and (ii) Type III calcite twinning.

Figure 4: Raman spectra and parameters. (A) Representative Raman spectrum showing G and D peaks, peak position, peak width, and peak intensities. (B) Cross-plot showing G-peak position against G-peak width for kerogen and graphitic material, after Muirhead et al. (2017a). Average values for samples in this study are plotted as white circles, with ranges for each sample indicated by black bars; all fall within the kerogen zone, demonstrating that carbon ordering has not progressed to the extreme of graphitization.

Figure 5: Raman I[d]/I[g] ratios with depth through the thrust-stacked stratigraphy. The shear zone of the overturned limb is marked in grey.

Figure 6: Details of Raman I[d]/I[g] ratios and strain indicators in the fold. (A) Simplified diagram to represent NW-SE cross-section through the fold, with upper, overturned, and lower limbs labelled. Depth through fold is marked. Sample locations are coloured according to twin type and strain ranking score (SRS). (B) I[d]/I[g] ratio plotted against transect length through fold. Points are averages of the 30 spectra obtained for each sample. Dashed lines denote approximate boundaries between upper, overturned, and lower limbs. (C) Box-and-whisker plot to show median values and interquartile ranges of I[d]/I[g] values for each limb.

Table 1: Strain indicators and strain ranking score from characteristics analysed in thin section across the fold structure. Factors included in the calculation of the strain ranking score are shaded in grey. The strain ranking score is a scale between 0 (no evidence of strain) and 10 (most strained sample), where the total (T) of E+D+A has been normalised to fit onto this scale, for ease of comparison.

Graphical Abstract (for review)

Carbon ordering in an aseismic shear zone: implications for Raman geothermometry and strain tracking

Lauren Kedar, Clare E. Bond, David Muirhead
University of Aberdeen

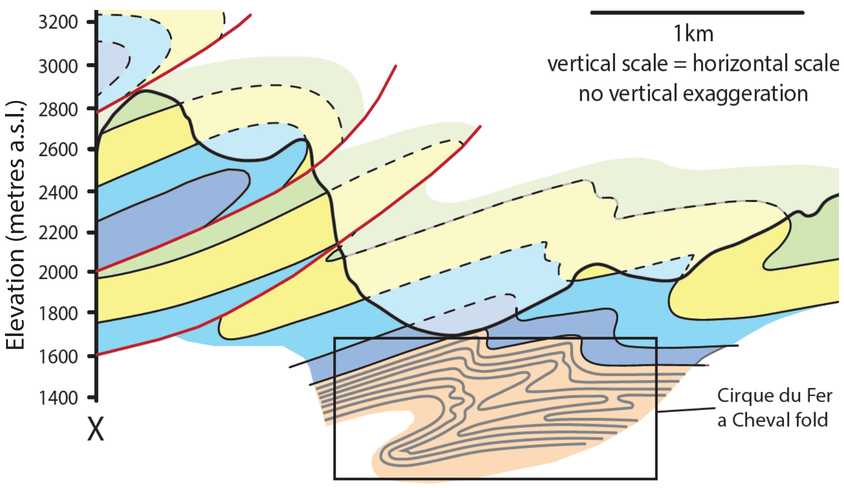

We consider a recumbent isoclinal fold consisting of Bajocian marls, whose overturned limb forms a 170m-thick shear zone. 26 samples were collected from across all three limbs, and prepared for Raman spectroscopy.

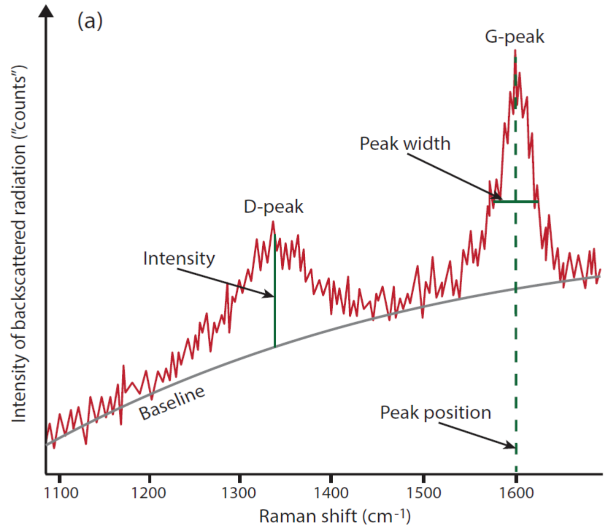

Samples were analysed using Raman spectroscopy to identify changes in peak intesnity ratios (I[d]/I[g]).

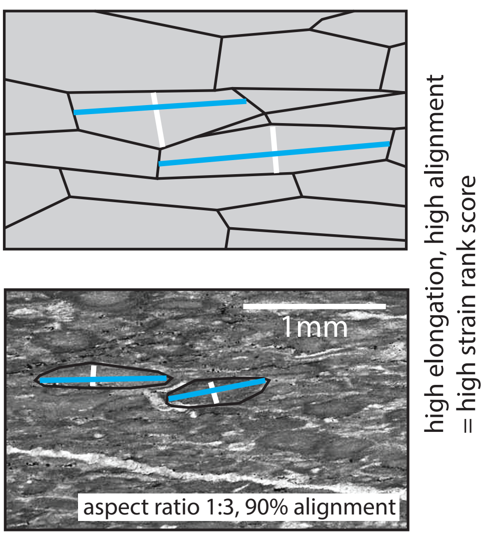

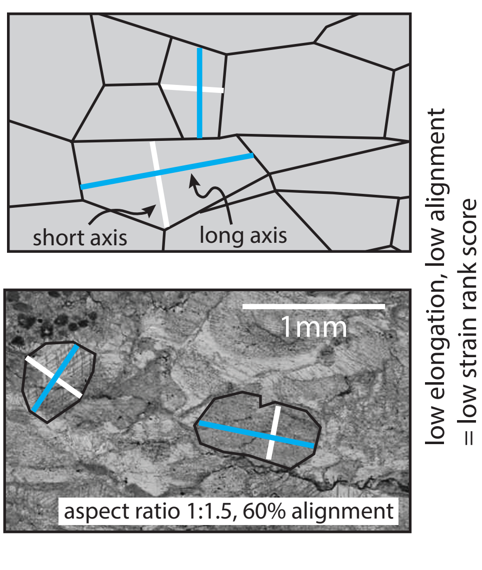

Samples were also prepared in thin section to enable optical analysis of micro-structures. A "strain rank score" was developed for comparison of strain intensity as indicated by grain elongation, grain alignment, frequency of dissolution seams and calcite twin type.

Samples taken from the over-turned limb had consistently higher strain rank scores, suggest-ing exposure to higher strain than those in the upper or lower limbs.

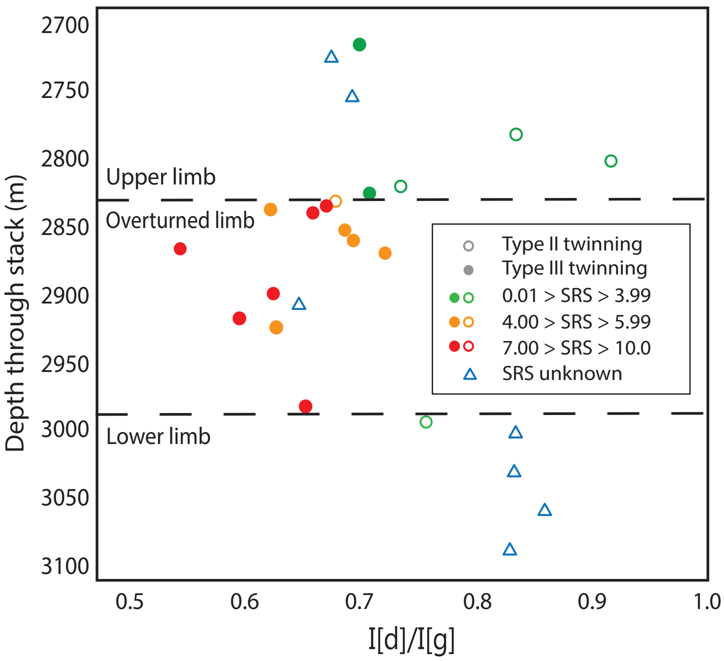

I[d]/I[g] ratios were compared across the fold structure. In the overturned limb there is a significant shift towards lower I[d]/I[g] values (average decrease of 23%), which correlates with consistent indicators of higher strain. This suggests that aseismic strain in a distributed shear zone can affect Raman spectral parameters.

IMPLICATIONS

- Strain-related carbon ordering can occur in distributed shear zones and not just on fault planes.
- Raman-based geothermometry has limited use in strained terranes, unless the strain-related signal can be isolated from that of temperature.

Figure 1

Click here to download Figure: Figure-1-Kedar-et-al.pdf

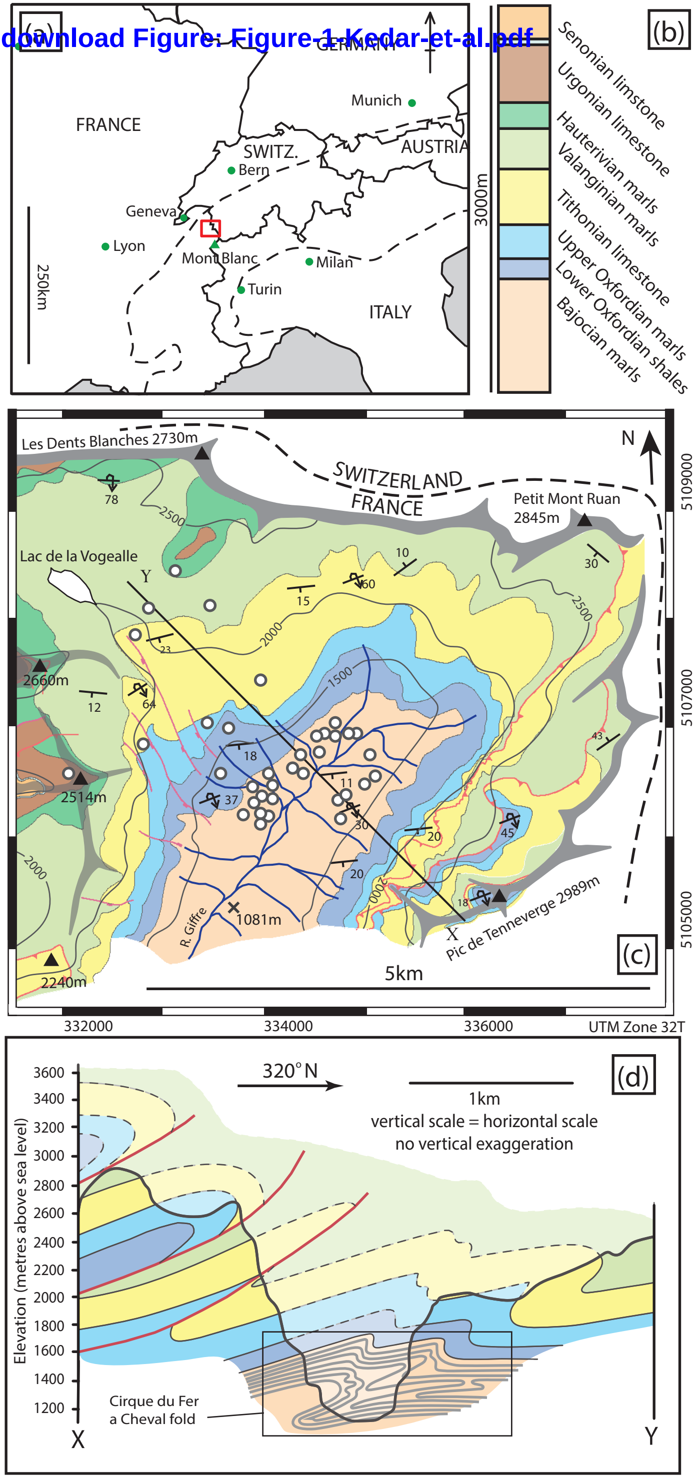

Figure 2 - reduced file size
Click here to download Figure: Figure2-low-res.pdf

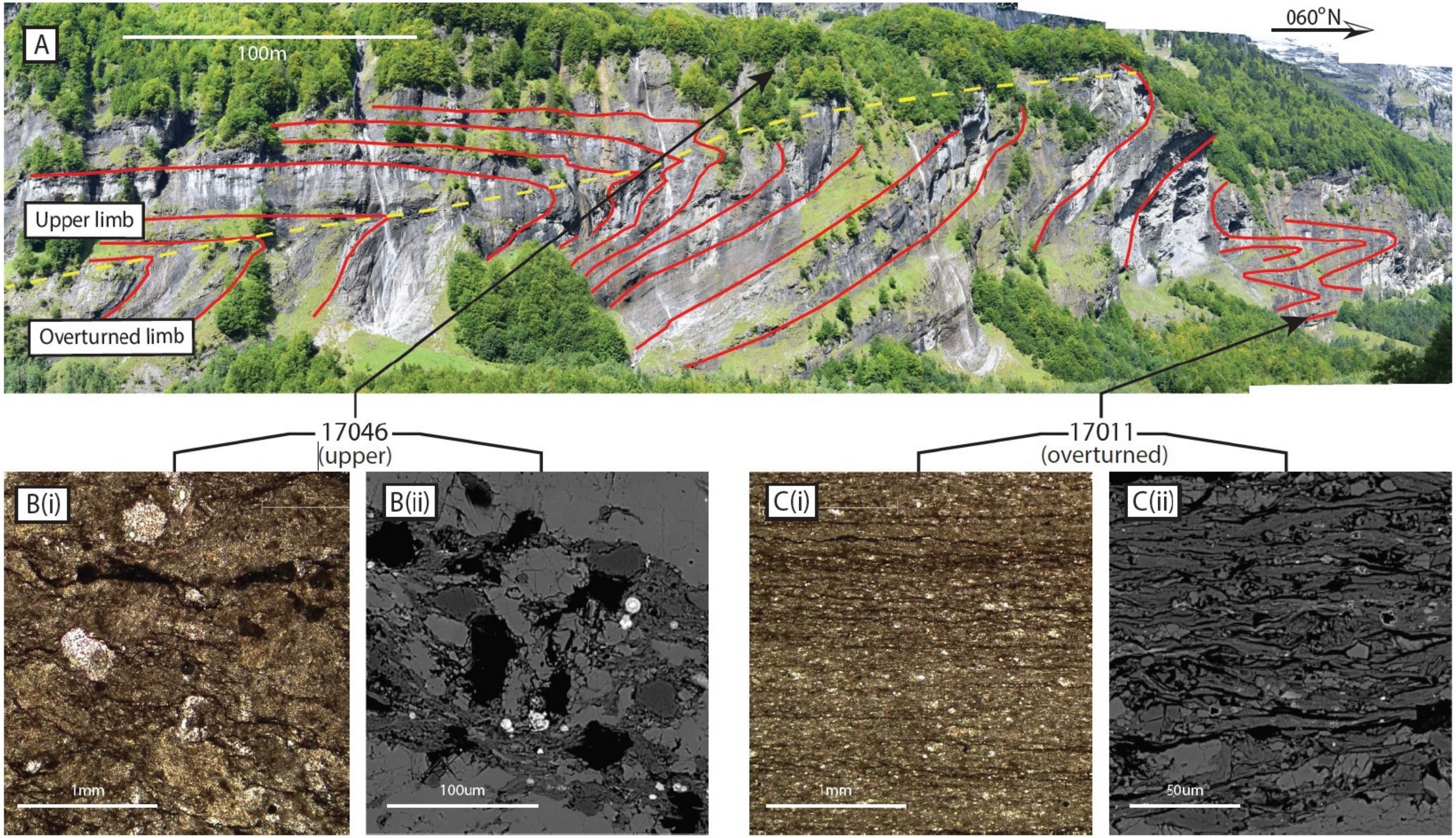

Figure 3

Click here to download Figure: Figure-3-Kedar-et-al.pdf

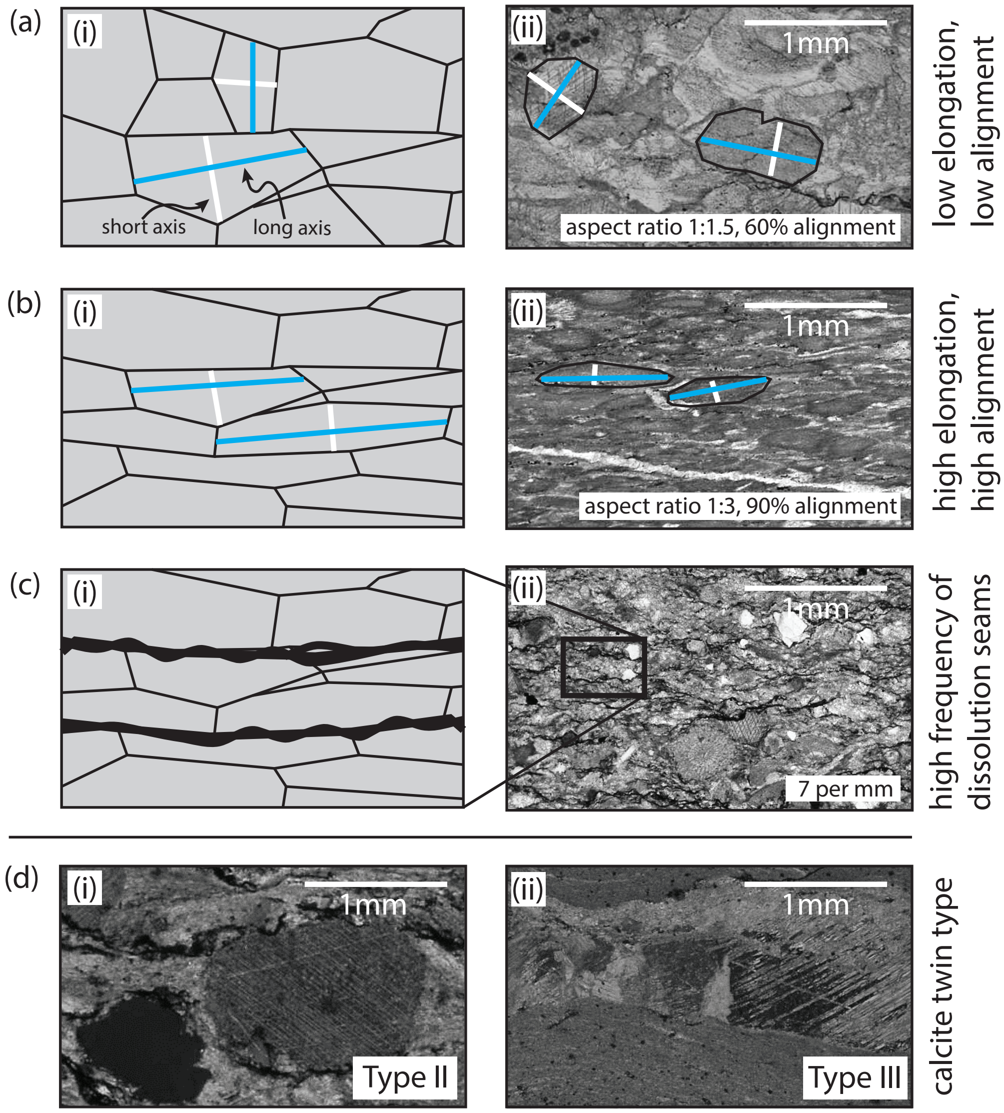

Figure 4

Click here to download Figure: Figure-4-Kedar-et-al.pdf

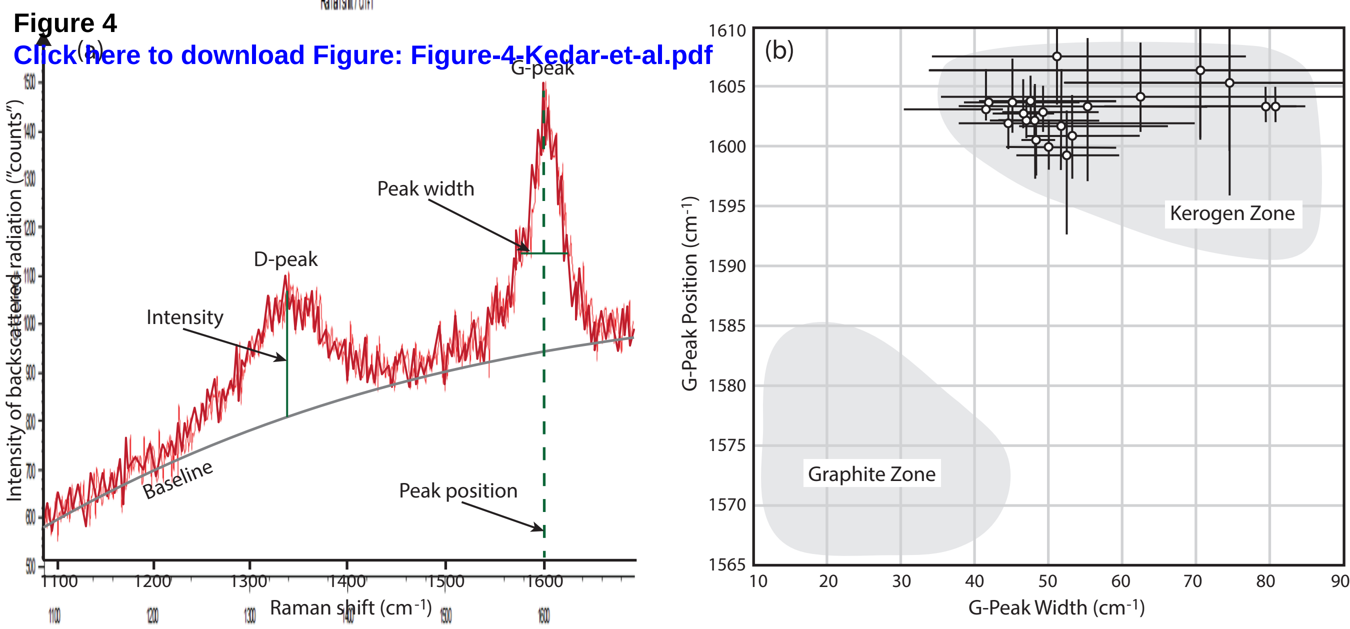

Figure 5

Click here to download Figure: Figure-5-Kedar-et-al.pdf

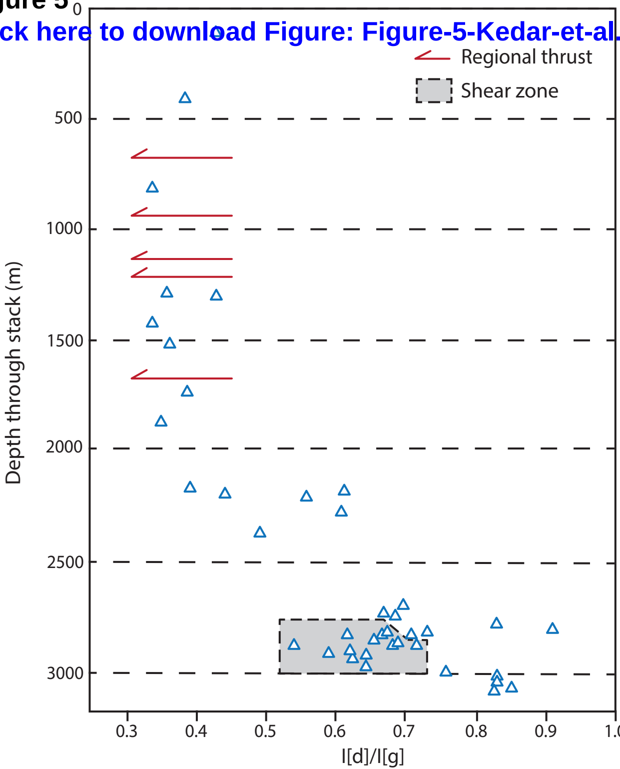

Figure 6

Click here to download Figure: Figure-6-Kedar-et-al.pdf

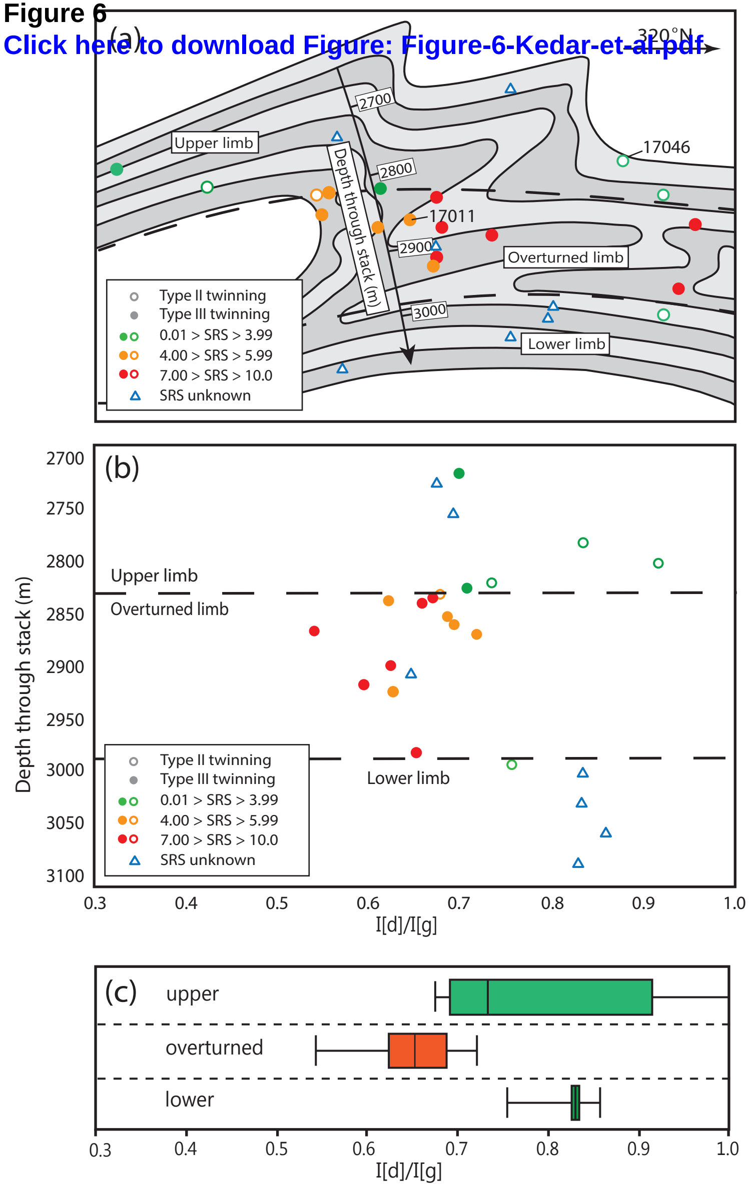

Figure 2 (high-resolution)

Table 1

Click here to download Table: Table-1.docx

Sample number	Limb	I[d]/I[g]	Transect Depth (m)	Calcite Twin Type	Calcite Elongation (*E*)		Freq. of Dissolution surfaces (*D*)		% Grain or Twin Alignment (*A*)	% Second Phase	Grain Size (mm)	Total E+D+A	Strain Ranking Score	Relative strain
					aspect ratio	weighted	per mm	weighted						
17021	upper	0.696063	2800	3	1.2	5	4.5	30	60	0	0.3	95	1.87	Low
18007	upper	0.673116	2810	ND†	ND	ND	ND	ND	ND	ND	ND	-	-	-
17029	upper	1.033372	2830	ND	ND	ND	ND	ND	ND	ND	ND	-	-	-
18006	upper	0.691537	2840	2	2	25	6	40	60	5	0.1	125	3.30	Low
17028	upper	0.831799	2870	2	1.2	25	3	20	50	10	0.5	75	0.91	Low
17027	upper	1.341459	2880	2	1.5	12.5	3	20	60	0	0.4	92.5	1.75	Low
17046	upper	0.913897	2890	2	1.2	5	4.5	30	40	10	0.5	75	0.91	Low
17009	upper	0.7327	2910	2	1.2	5	3	20	50	5	0.5	75	0.91	Low
18005	upper	0.7053	2916	3	1.5	12.5	6	40	50	2	0.1	102.5	2.22	Low
17006	upper	0.676249	2920	2	1.5	12.5	10.5	70	80	2	0.1	142.5	4.14	Medium
18003	overturned	0.670268	2924	3	4	75	6	40	80	20	0.5	195	6.65	High
17007	overturned	0.622239	2926	3	2	25	3	20	60	20	0.5	145	4.26	Medium
18004	overturned	0.65857	2928	2.5††	2	25	12	80	80	10	0.2	185	6.17	High
18002	overturned	0.685537	2944	3	3	50	3	20	100	5	1.5	170	5.45	Medium
17001	overturned	0.692743	2950	3	2	25	7.5	50	90	0	0.1	165	5.21	Medium
17005	overturned	0.54322	2958	3.5	2	25	7.5	50	80	5	2	155	4.74	Medium
17011	overturned	0.720705	2960	3	3	50	15	100	90	0	0.05	265	10.0	High
17030	overturned	0.624039	2990	ND	ND	ND	ND	ND	ND	ND	ND	-	-	-
18062	overturned	0.645499	3000	3	5	100	4.5	30	90	30	1	220	7.85	High
18060	overturned	0.594851	3010	3	2	25	7.5	50	70	0	0.2	145	4.26	Medium
18061	overturned	0.626713	3016	3	3	50	10.5	70	70	0	0.3	190	6.41	High
17003	lower	0.754029	3090	2.5	1.5	12.5	1.5	10	90	0	0.2	112.5	2.70	Low
18020	lower	0.832336	3100	ND	ND	ND	ND	ND	ND	ND	ND	-	-	
18019	lower	0.830863	3130	ND	ND	ND	ND	ND	ND	ND	ND	-	-	
18016	lower	0.857968	3160	ND	ND	ND	ND	ND	ND	ND	ND	-	-	
18001	lower	0.827443	3190	ND	ND	ND	ND	ND	ND	ND	ND	-	-	

†ND = No Data. This is shown where no thin section was available, but Raman spectral data was obtained, and field/hand specimen observations were made.

††Where a sample exhibits Type II and Type III twins in different calcite grains, the twin type is listed as 2.5. Similarly, as at least one grain had Type IV twins, sample 17005 is listed as 3.5.

TABLE 1: STRAIN INDICATORS AND STRAIN RANKING SCORE